Separation and Purification Technology 395 (2026) 137682

Contents lists available at ScienceDirect

Separation and Purification Technology

journal homepage: www.elsevier.com/locate/seppur

Enhanced capacity and selectivity of carbon quantum dots integrated NU-1000 MOF for CO_2 capture

Xujing Chen [a,b], Guanhong Lu [a], Shijie Yang [a,b], Xiaoyu Duan [a], Shiqian Zhou [a,b], Xiao Wang [a], Gansheng Shi [a], Jing Sun [a,*]

[a] State Key Lab of High Performance Ceramics and Superfine Microstructure, Shanghai Institute of Ceramics, Chinese Academy of Sciences, 585 Heshuo Road, Shanghai 201899, China
[b] University of Chinese Academy of Sciences, 19 (A) Yuquan Road, Beijing 100049, China

ARTICLE INFO

Editor name: Yeshui Zhang

Keywords:
NU-1000
Carbon quantum dots
Metal-organic frameworks
CO_2 adsorption
Direct air capture

ABSTRACT

In recent years, Metal-Organic Frameworks (MOFs) have demonstrated significant potential as adsorbents for CO_2 capture, particularly in direct air capture (DAC). However, their adsorption capacity and the selectivity still require further enhancement. Herein, we report the synthesis of CQDs/NU-1000 composites by incorporating carbon quantum dots (CQDs) into NU-1000 framework. The structure, morphology, and pore characteristics of the resulted composites were investigated by various characterization methods. The composite with the highest CO_2 uptake, 1.0 CQDs/NU-1000, exhibits adsorption capacity of 1.99 mmol·g^{-1} at 0.1 MPa and 25 °C, which is 1.79 times higher than that of pristine NU-1000. The 1.0CQDs/NU-1000 composite maintains a CO_2 adsorption capacity of 1.89 mmol·g^{-1} even under 100% relative humidity. Dynamic breakthrough experiments conducted under simulated air conditions further demonstrate that this composite delivers a dynamic adsorption capacity approximately fivefold higher and a CO_2/N_2 selectivity about fourfold higher than those of the pristine material. TPD and in situ FTIR results reveal that the introduction of CQDs enhances the Lewis basicity of the open metal sites in NU-1000 and increases the surface hydroxyl oxygen content, and the resulting formation of carbonate species is the main contributor to the enhanced chemisorption capacity for CO_2. This work offers an effective strategy to enhance the CO_2 capture performance of MOF-based adsorbents, and provides insights for the design of high-performance materials for CO_2 separation and DAC technology.

1. Introduction

To address the greenhouse effect caused by the increased atmospheric CO_2 levels [1], carbon capture technologies are from conventional point source capture to an integrated system of carbon capture, utilization and storage (CCUS) [2,3]. Within this system, direct air capture (DAC) is a promising strategy for achieving net negative carbon emissions [4,5], but the extremely low CO_2 concentration in ambient air of about 400 ppm necessitates high selectivity and capacity for sorbents. Although liquid amine absorption has been widely employed for flue gas CO_2 capture [6], problems such as equipment corrosion, high regeneration energy consumption, and amine degradation [7] make solid sorbents a more promising option for advancing CO_2 capture technologies.

Among various solid sorbents such as zeolites [8], activated carbons [9], and porous organic polymers [10], covalent-organic frameworks [11], metal-organic frameworks (MOFs) stand out because their high surface areas, tunable pore structures and tailorable chemical environments enable strong interactions with CO_2 [12,13]. For instance, some studies have assembled MOFs (e.g., ZIF-8 and its functionalized derivatives) onto nanofiber substrates to address the issue of low gas mass transfer efficiency of MOFs in practical applications. [14–16] However, under DAC conditions, issues such as the limited adsorption capacity, insufficient thermal stability, and moisture sensitivity of many pristine MOFs have not yet been resolved. [12,17,18]. Therefore, while maintaining the water and thermal stability of MOFs, improving the pore structures and local chemical environments of stable MOFs is essential for achieving higher CO_2 adsorption capacity and selectivity.

Zirconium-based MOFs such as UiO-66 [19], MOF-808 [20] and NU-1000 [21] are known for their exceptional thermal, chemical and water stability, making them promising candidates for energy and environmental applications [22,23]. NU-1000 features a hierarchical pore structure and unsaturated coordinated Zr_6 clusters, which are favorable

* Corresponding author.
E-mail address: jingsun@mail.sic.ac.cn (J. Sun).

https://doi.org/10.1016/j.seppur.2026.137682
Received 5 January 2026; Received in revised form 28 February 2026; Accepted 19 March 2026
Available online 20 March 2026

for CO_2 adsorption and related transformations [24–27]. Although modification strategies for MOF-based solid sorbents such as the introduction of amino groups, organic amines or metal oxide nanoparticles can enhance their CO_2 adsorption performance, they still face limitations including amine volatilization and deactivation, nanoparticle aggregation and complex synthesis procedures [12,23,28–31]. Therefore, it is particularly crucial to develop a simple, controllable, and efficient modification strategy to overcome these issues and further enhance the CO_2 capture performance of MOFs.

Carbon quantum dots (CQDs) are zero-dimensional carbon-based nanomaterials with small particle sizes, excellent dispersibility, and stable chemical properties. Their surfaces are rich in oxygen-containing functional groups [32]. In composite systems, CQDs can not only provide additional adsorption or reaction sites but also modulate the local electronic structure and polarity of the host material [33,34]. Davood et al. found that a nitrogen-doped carbon quantum dots/reduced graphene oxide nanocomposite could improve the micropore/mesopore ratio of MOFs and enhance CO_2 adsorption [35]. Inspired by this, we propose a simple and controllable CQDs doping strategy to modulate the pore structure and microenvironment of NU-1000, thereby enhancing its CO_2 capture performance under DAC conditions for the first time. CQDs and NU-1000 were first synthesized separately; then a series of CQDs/NU-1000 composites were prepared via a simple impregnation method and systematically investigated their CO_2 adsorption behavior. Static adsorption isotherms and dynamic breakthrough experiments under simulated air conditions both demonstrate that the introduction of CQDs significantly enhances the CO_2 adsorption capacity and improves CO_2/N_2 dynamic breakthrough selectivity. Brunauer-Emmett-Teller (BET) analysis indicates that the incorporation of CQDs optimizes the specific surface area and pore structure of the composites, while CO_2 temperature programmed desorption (CO_2-TPD) and in-situ Fourier transform infrared spectroscopy (in situ FTIR) further confirm that CQDs promote the formation of carbonate species, thereby strengthening the chemical interaction between CO_2 and the adsorbent. This study provides a simple and effective strategy for tuning the structure of NU-1000-based MOF materials and enhancing their CO_2 adsorption performance.

2. Experimental section

2.1. Materials and chemicals

All reagents were obtained from commercial sources and used as received without further purification. *N*,*N*-dimethylformamide (DMF, 99%, AR), 1,3,6,8-tetrakis(p-benzoic acid) pyrene (H_4TBAPy, 99%, AR), zirconyl chloride octahydrate ($ZrOCl_2{\cdot}8H_2O$, 99%, AR), urea (99%, AR), and silicon dioxide (SiO_2, 99%, AR) were purchased from Shanghai Adamas Reagent Co., Ltd. Citric acid monohydrate (99%, AR) was supplied by China National Medicines Corporation Ltd. Ethanol (EtOH, 99%, AR) and acetone (99%, AR) were obtained from Shanghai Lingfeng Chemical Reagent Co., Ltd. Deionized water(DI) was produced with ultrapure water system (Tondino Scientific Co., Ltd., Shanghai). High-purity gases, including Ar (99.99%), N_2 (99.99%), and CO_2 (99.99%), were supplied by from Shanghai Guanglin Gas Co., Ltd.

2.2. Synthesis of adsorbents

2.2.1. Synthesis of CQDs

CQDs were synthesized via a modified hydrothermal method based on procedures previously reported procedures [36]. Citric acid (1 g) and urea (1 g) were dissolved in 15 mL of deionized water (DI) under ultrasonic agitation. The solution was transferred to a 25 mL PTFE-lined autoclave and heated at 180 °C, for 6 h. After being cooled to room temperature, the dark brown suspension was centrifuged at 10,000 rpm for 20 min. The as-obtained supernatant was collected and dried at 80 °C, to get CQDs powder (See Scheme 1).

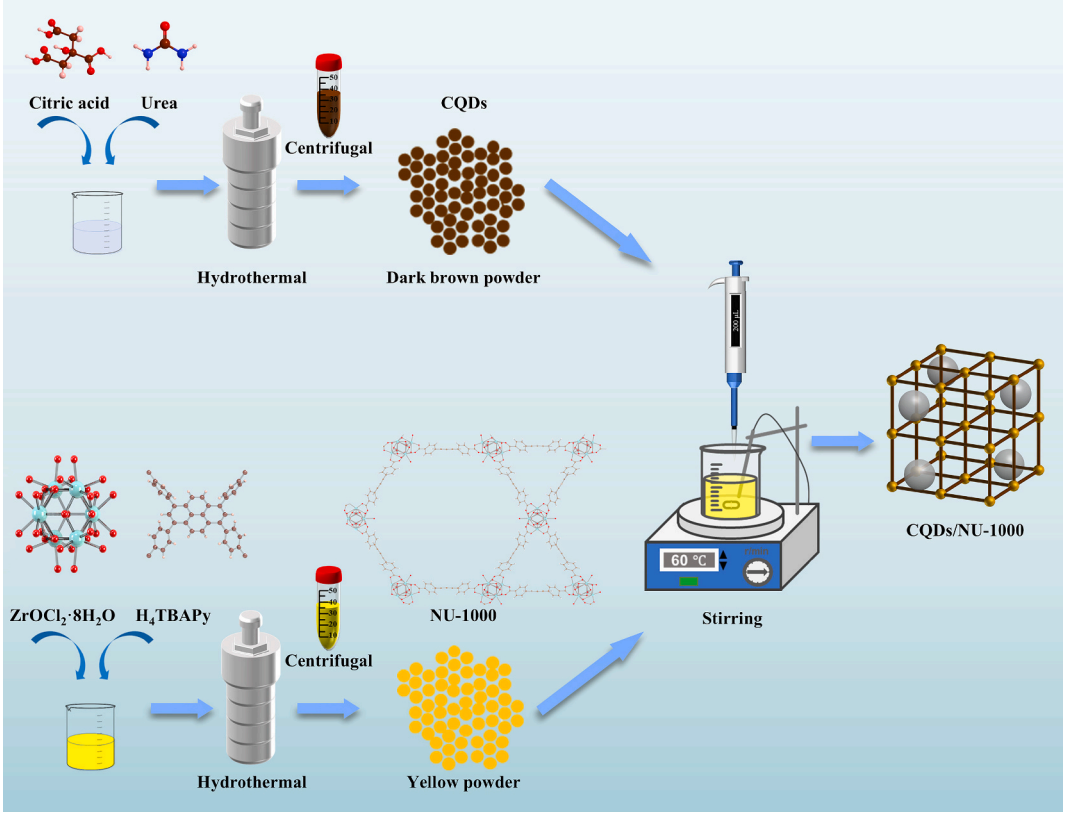

Scheme 1. Schematic illustration of the preparation process of the CQDs/NU-1000 composite.

2.2.2. Synthesis of NU-1000

NU-1000 was synthesized following a slightly modified literature method [37]. Zirconyl chloride octahydrate (388 mg) and benzoic acid (10.8 g) were dissolved in 28 mL of DMF. Separately, H_4TBAPy (160 mg) was dissolved in 4 mL of DMF. Both solutions were ultrasonicated, preheated at 80 °C, for 1 h, cooled to room temperature, and mixed together. The mixture was heated at 100 °C, for 16 h.

The yellow precipitate was collected by centrifugation and washed three times with DMF. The as-obtained solid was redispersed in 50 mL of DMF, treated with 2 mL of 8 M HCl, and heated at 100 °C, for 12 h. The product was washed three times with DMF and subsequently with acetone wash for three times. It was dried under vacuum at 80 °C, for 12 h, ground into a fine powder, and finally activated at 120 °C, for 12 h under vacuum.

2.2.3. Synthesis of CQDs/NU-1000

100 mg of activated NU-1000 powder was dispersed in 20 mL of ethanol (solution A). The CQDs were dissolved in ethanol to make a 5 mg/mL suspension (solution B). 1.0 mL of solution B was added dropwise into solution A, and the mixture was stirred at 40 °C, for 12 h. The solid was then separated by centrifugation, washed several times with ethanol, and dried under vacuum at 100 °C, for 12 h. The final sample is referred to as 1.0CQDs/NU-1000. Using the same procedure but varying the volume of solution B, additional composites were obtained and marked as xCQDs/ NU-1000 (x = 0.2, 0.6, 1.5, 2.0 mL), Based on the added volumes of the CQDs solution (5 mg/mL), the nominal mass loadings of CQDs in the resulting composites were calculated to be 1.0, 3.0, 5.0, 7.5, and 10.0 wt%, respectively.

2.3. Characterization and testing methods

Scanning electron microscopy (SEM) analysis was performed using a field-emission scanning electron microscope FEI Magellan 400. Transmission electron microscopy (TEM) and high-resolution transmission electron microscopy (HRTEM) images were obtained using a Hitachi HF5000 electron microscope. Powder X-ray diffraction (PXRD) patterns were recorded using a Bruker D8 ADVANCE diffractometer with Cu Kα radiation (λ = 0.15418 nm) at room temperature. Brunauer-Emmett-Teller (BET) surface area measurements and CO_2 adsorption isotherms were measured using JW-BK100 instruments. X-ray photoelectron spectroscopy (XPS) was conducted on an ESCAlab 250 spectrometer (Thermo-VG Scientific). Temperature-programmed desorption (TPD) measurements were carried out using a PCA-1200 chemisorption analyzer. Thermogravimetric analysis (TGA) was performed on a Netzsch STA 449 F3 thermal analyzer. In situ diffuse reflectance infrared Fourier transform (in situ FTIR) spectra were collected using a Thermo Fisher iN10/iZ10 system. $CO_2/N_2/O_2$ dynamic breakthrough tests were conducted on a BTsorb-100 SMPPRO instrument to evaluate the DAC performance The adsorption performance under different humidity conditions was evaluated using an ESPEC SH-222 bench-top temperature & humidity Chamber.

3. Result and discussion

3.1. Characterization of materials

3.1.1. Morphology

Fig. 1 shows the morphological features of pristine NU-1000 and 1.0CQDs/NU-1000, the latter of which exhibits the most significant

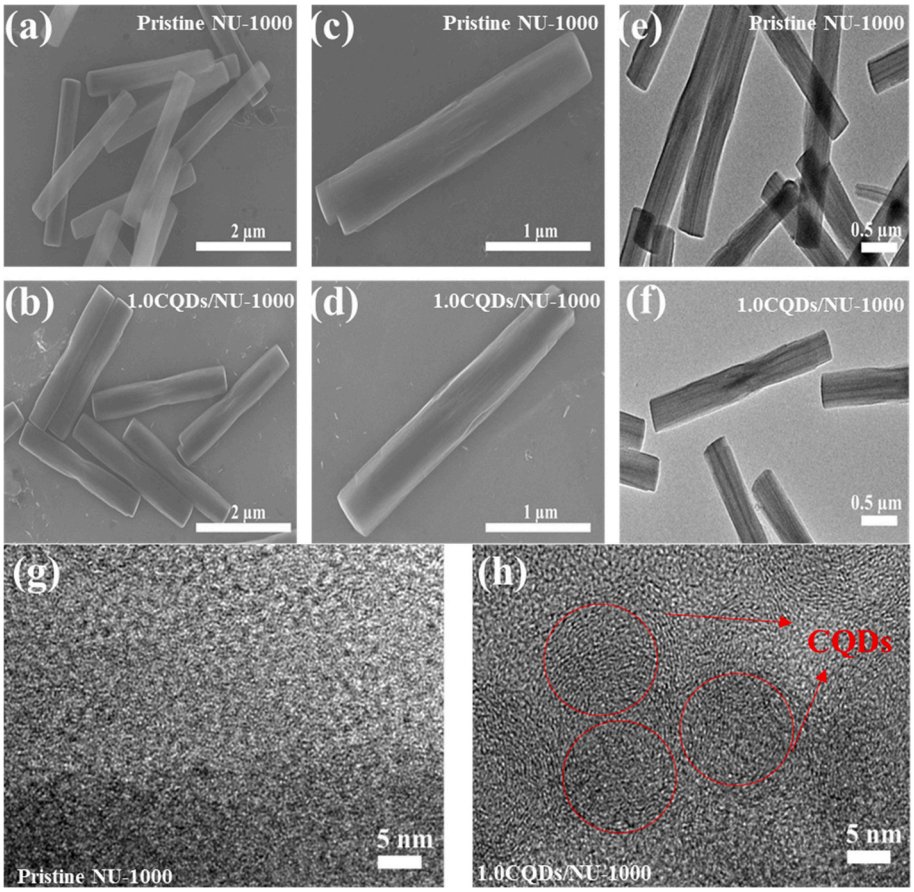

Fig. 1. SEM images of pristine NU-1000 and 1.0CQDs/NU-1000(a-d); TEM images of pristine NU-1000(e) and 1.0CQDs/NU-1000(f); HRTEM images of pristine NU-1000(g) and 1.0CQDs/NU-1000(h).

enhancement in CO_2 adsorption performance. SEM images of pristine NU-1000 (Fig. 1a and c) reveal a regular rod-like crystalline morphology characterized by uniformly distributed particles, smooth surfaces, and well-defined edges [21]. After the introduction of CQDs (Fig. 1b and d), the composite maintains its well-defined rod-like structure. No crystal collapse or discernible interfacial defects were observed, indicating that the combining process does not influence the structural integrity of the NU-1000 framework.

In the SEM and conventional TEM images, CQDs are not directly observable, primarily due to their ultrasmall dimensions (typically <10 nm) falling below the effective spatial resolution limit of the techniques [38]. This is consistent with previous reports, which note that CQDs are typically indistinguishable via conventional SEM imaging. In contrast, HRTEM provides more direct evidence of the successful incorporation. In the HRTEM image of 1.0CQDs/NU-1000 (Fig. 1h), several spherical dark spots were observed on the surface of the crystals [39]. These spots, which cannot be observed in pristine NU-1000, can be attributed to CQDs attached to the surface and near-surface regions of NU-1000. Meanwhile, the rod-like crystals still maintain their intact morphology (Fig. 1f), with sharp crystal edges and no signs of collapse or fracture, further confirming that the introduction of CQDs does not detrimentally affect the NU-1000 framework. This structural robustness is beneficial for maintaining open pore channels and is thus crucial for preserving and enhancing the CO_2 adsorption performance of the material.

3.1.2. Crystal structure

XRD patterns (Fig. 2a) were recorded to examine the phase composition and crystallinity of NU-1000 and the CQDs/NU-1000 composites. The characteristic diffraction peaks of all samples, both before and after the incorporation of with CQDs, are in good agreement with the simulated pattern. Specifically, the primary diffraction peaks at $2\theta = 5.1^o$, 7.4^o and 10.2^o remain consistent across all samples, and no additional peaks belonging to other phases were detected [21,37]. However, the enlarged XRD patterns **(Fig. S1)** show a slight shift in the characteristic peaks of the CQDs/NU-1000 composites relative to pristine NU-1000. According to Bragg's law, this shift indicates a minor change in the interplanar spacing, suggesting a slight lattice distortion of the NU-1000 framework induced by CQDs doping [40]. Similar results associated with the post-synthetic modification or guest encapsulation have been well-documented [40,41]. Overall, the XRD results confirm that the long-range order of NU-1000 is preserved, with the composites retaining excellent crystallinity without undergoing phase transformation or framework collapse.

3.1.3. Specific surface area and pore size distribution

To gain more deeper insights into the influence of the CQDs loading amount on the pore structure of the composites, N_2 adsorption-desorption isotherms were recorded for pristine NU-1000 and the CQDs/NU-1000 samples (Fig. 2b and c), and the corresponding parameters are summarized in Table 1. All samples exhibit typical type IV isotherms, indicating that the materials are predominantly mesoporous and possess a hierarchical pore structure, which is consistent with previous reports on NU-1000 [21,37].

Pristine NU-1000 exhibits a BET surface area of 1505 m^2g^{-1} and a pore volume of 1.23 cm^3/g. The pore size distribution derived from the HK and SF methods reveals micropores at approximately 0.6 nm, which match well with the kinetic diameter of CO_2 (0.33 nm), thereby provides abundant and effective adsorption space for CO_2 molecules [42]. In

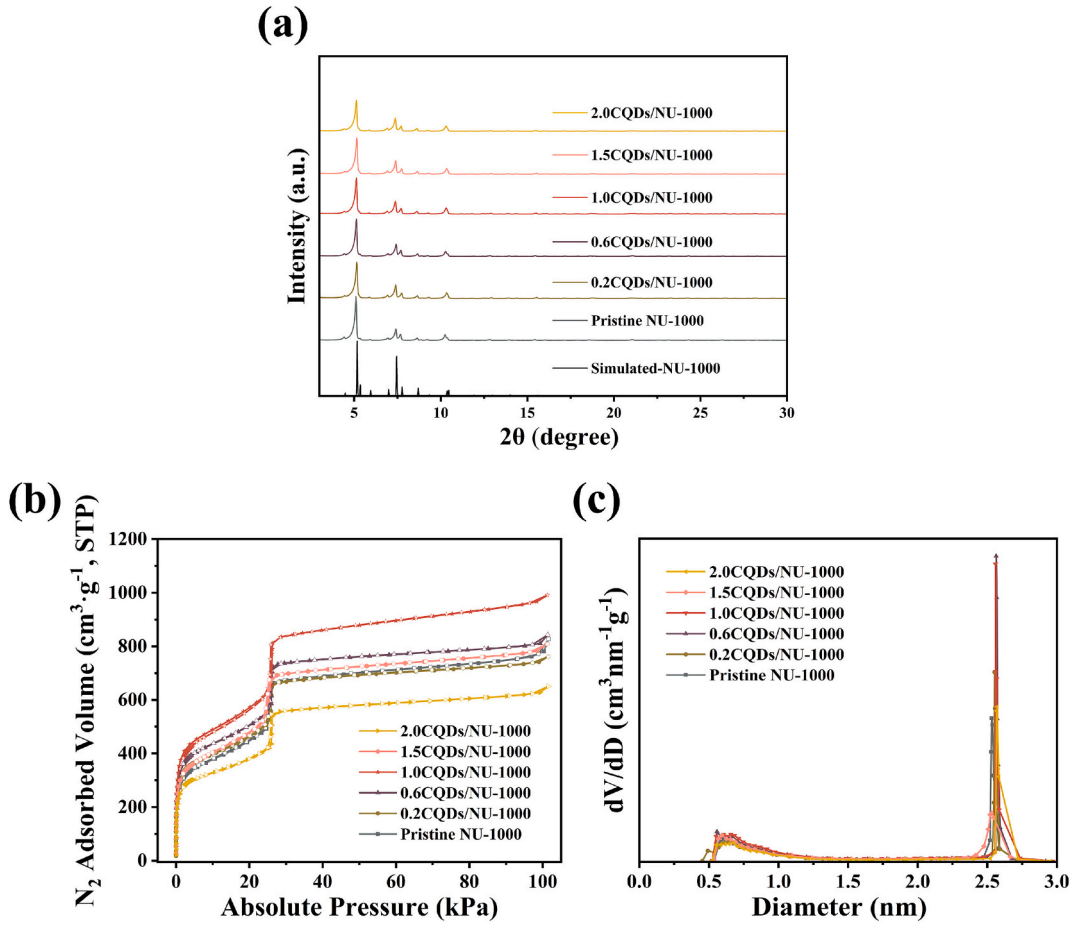

Fig. 2. Pristine NU-1000 and series of CQDs/NU-1000 of (a) XRD patterns, (b) N_2 adsorption isotherms of NU-1000 and a series of CQDs/NU-1000 at 77 K, (c) Pore size distribution of NU-1000 and series of CQDs/NU-1000.

Table 1
The physical structural properties of samples.

Samples	S_{BET}[a](m^2/g)	V^b_{total}(cm^3/g)	V^c_{micro}(cm^3/g)	V^d_{meso}(cm^3/g)	$D^e_{average}$(nm)
Pristine NU-1000-	1505	1.23	0.58	0.65	3.28
0.2CQDs/NU-1000	1528	1.17	0.50	0.67	2.95
0.6CQDs/NU-1000	1737	1.28	0.54	0.74	2.95
1.0CQDs/NU-1000	1937	1.53	0.69	0.84	3.12
1.5CQDs/NU-1000	1599	1.23	0.54	0.69	3.09
2.0CQDs/NU-1000	1308	0.99	0.44	0.55	3.03

[a] BET specific surface; [b] Total pore volume measured at $P/P_0 = 0.99$; [c] Micropore volume calculated using the BJH method; [d] Mesopore volume calculated using the BJH method; [e] Average pore diameter calculated using the HK/SF method.

addition, the presence of mesopores around 2.5 nm offers favorable diffusion pathways for efficient gas transport.

To deeply understand the relation of physical structural properties and loading, the pore size distribution (PSD) was further analyzed. While the overall trends are shown in Fig. 2c, the separated HK profiles **(Fig. S3)** clearly detail the changes of pore distribution. Both micropores (~0.6 nm) and mesopores (~2.5 nm) were found in the NU-1000 samples. The micropore (< 2 nm) remains largely unchanged with CQDs loading. Given that the sizes of CQDs are mostly larger than 2 nm (TEM results in Fig.1h**)**, the deposition of CQDs in the micropores is prohibited while the mesopores provide possibilities for the residence of CQDs. With the dosage of CQDs increased, the mesopore peak firstly increased (pristine NU-1000 to 1.0CQDs/NU-1000 and then decreased (1.5CQDs/NU-1000 and 2.0 CQDs/NU-1000). This is due to the fact that the entering of a small amount of CQDs into the mesopores may lead to the generation of defects, thereby resulting in an increase in mesoporous capacity and providing new active sites for the adsorption of CO_2 [43]. Among all the samples, 1.0CQDs/NU-1000 (5 wt% CQDs loading) exhibit the optimal CO_2 adsorption capacity, which is in accordance with its high specific surface area and the large total pore volume **(Table 1)**. When further increasing the dosage of CQDs, the blockage of mesopores happened, resulting in both the decreased of mesopores and the deteriorated CO_2 adsorption performance.

With the increase in CQDs doping, the surface area of the composites initially increases and subsequently decreases, following the same trend as the CO_2 adsorption capacity shown in Table 2. The presence of CQDs increases the roughness of the pore surfaces and creates additional contact interfaces, leading to a higher effective surface area. However, at a higher CQDs loading, the surface area decreases, which is primarily ascribed to the partial blockage of the pores by CQDs [44]. The blocked pores limit the access of CO_2 molecules and are unfavorable for adsorption. These results indicate that CQDs are successfully incorporated into the NU-1000 framework and alter the surface area and porosity of the material.

Taken together with the SEM and PXRD results, it can be concluded that CQDs are predominantly distributed on or near the pore channels of NU-1000. They slightly modulate the local pore structure and surface environment while maintaining the long-range order and open channels of the framework. This provides a favorable structural foundation for the enhancement of both physical adsorption and surface interactions during CO_2 capture.

Table 2
The static adsorption performance of samples.

Samples	Temperature (°C) /pressure (kPa)	CO_2 adsorption ($mmol \cdot g^{-1}$)	Percentage Increase
Pristine NU-1000	25/100	1.11	N/A
0.2CQDs/NU-1000	25/100	1.46	31.5%
0.6CQDs/NU-1000	25/100	1.85	66.6%
1.0CQDs/NU-1000	25/100	1.99	79.2%
1.5CQDs/NU-1000	25/100	1.68	51.4%
2.0CQDs/NU-1000	25/100	1.34	20.7%

3.1.4. Elemental composition and chemical state analysis

X-ray photoelectron spectroscopy (XPS) was performed to investigate the effect of CQDs incorporation on the surface valence states and electronic structure of the material. As shown in Fig. 3a, the survey spectrum displays characteristic peaks for zirconium (Zr) 3d, carbon (C) 1 s, and Oxygen (O) 1 s at binding energies of approximately 182.9, 284.9 and 532.7 eV, respectively. The high-resolution spectrum for these elements shown in Figs. 3b-d.

The high-resolution Zirconium (Zr) 3d spectrum were used to analyze the chemical state and electronic environment of Zr in pristine NU-1000 and 1.0CQDs/NU-1000. As shown in Fig. 3d, pristine NU-1000 exhibits two characteristic peaks at 185.6 eV (Zr $3d_{3/2}$) and 183.3 eV (Zr $3d_{5/2}$), corresponding to Zr(IV) in the Zr_6—O cluster, while the corresponding peaks of 1.0CQDs/NU-1000 appear at 185.3 eV and 182.9 eV [45]. This shift (~ 0.3–0.4 eV) signifies a meaningful increase in the local electron density around the Zr_6 clusters. Notably, the well-preserved peak symmetry and the constant spin-orbit splitting confirm that the Zr sites maintain their Zr (IV) oxidation state rather than undergoing a formal reduction. This phenomenon is attributed to interfacial electronic redistribution between the CQDs and the MOF framework. The electron-rich, π-conjugated structure of the CQDs induces electronic polarization at the interface, thereby enriching the electron cloud around the Zr centers. This modulation effectively modulates the Lewis acidity and polarizing ability of the the Zr sites and facilitates the polarization of CO_2 molecules, which is beneficial for the enhanced CO_2 adsorption performance observed in the composite.

To further confirm the structural integrity of the organic linker during synthesis and composite formation, the binding energies of carbon (C) species were analyzed. The high-resolution C 1 s spectrum **(**Fig. 3b**)** can be deconvoluted into three main peaks at 284.8, 286.5 and 288.8 eV, corresponding to C-C/C=C, C—O and C═O species, respectively [46]. These signals originate from the aromatic rings and carboxyl groups of the H_4TBAPy linker. The results indicate that the organic linker does not undergo discernible degradation during the synthesis and post-treatment processes, and its fundamental chemical structure is well-preserved.

The Oxygen (O) 1 s spectrum **(**Fig. 3c**)** were further analyzed to identify the different oxygen species on the material surface. The O 1 s spectrum of 1.0CQDs/NU-1000 can be deconvoluted into three peaks at 530.7, 532.2 and 533.3 eV, which are assigned to lattice oxygen (O_{lat}), adsorbed oxygen (O_{ads}) and surface hydroxyl oxygen (-OH), respectively [46]. Compared with pristine NU-1000, 1.0CQDs/NU-1000 shows a notable increase in the peak area of hydroxyl oxygen (533.3 eV) and a concomitant decrease in the peak area of adsorbed oxygen (532.2 eV). This indicates that the introduction of CQDs promotes the formation of more chemically bonded oxygen-containing functional groups such as -OH on the surface, while reducing the amount of weakly adsorbed oxygen/water molecules. Surface hydroxyl oxygen can act as active adsorption sites for CO_2 and enhance the affinity of the material toward CO_2 molecules through Lewis acid-base interactions and hydrogen bonding, which is highly favorable for CO_2 adsorption.

XPS results demonstrate that CQDs were successfully incorporated into NU-1000. While the framework structure remains intact, the CQDs doping modulates the electronic environment of the Zr sites and

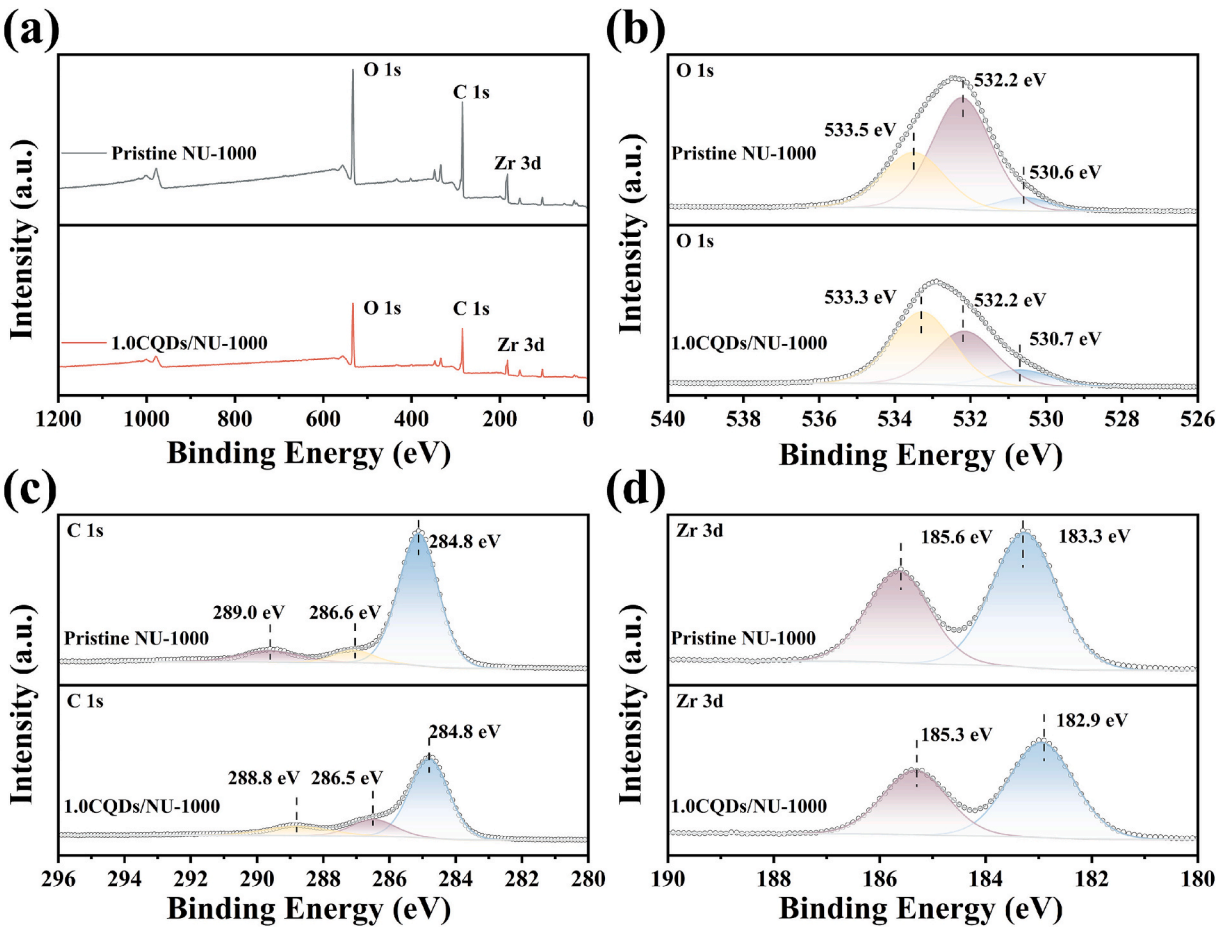

Fig. 3. XPS spectrum (a)survey; high-resolution spectra of C 1 s (b), O 1 s(c), and Zr 3d (d).

increases the abundance of oxygen-containing functional groups on the surface. These synergistic effects play an important role in the enhanced CO_2 adsorption performance of the composite.

3.2. CO_2 adsorption performance

3.2.1. CO_2 static adsorption performance

CO_2 adsorption performance of pristine NU-1000 and a series of CQDs/NU-1000 composites with varying CQD loadings were evaluated. Static CO_2 adsorption tests were conducted at 0 °C and 25 °C, and the results are shown in Fig. 4a and b. Notably, sample 1.0 CQDs/NU-1000 exhibits the highest CO_2 adsorption capacity, demonstrating superior performance compared to the other samples. Therefore, we mainly focuses on comparing the sample 1.0 CQDs/NU-1000 with pristine NU-1000.

According to the static adsorption curves at 25 °C presented in Table 2, it can be observed that when the CQDs loading increases from 0.2 to 1.0 mL, the CO_2 adsorption capacity rises from 1.11 to 1.99 $mmol{\cdot}g^{-1}$. However, with a further incremental increase in CQDs, the CO_2 adsorption capacity gradually decreases. This trend is consistent with the variation in BET surface areas. An excessive amount of CQDs may block the pores or form aggregates, leading to a decline in the CO_2 adsorption capacity performance [44].

To better understand the role of CQDs in CO_2 adsorption, CQDs/SiO_2 composite was prepared as a control sample. As shown in Fig. 4c, under the same test conditions, The CO_2 adsorption capacity of 1.0 CQDs/SiO_2 is 0.036 $mmol{\cdot}g^{-1}$ at 25 °C and 100 kPa, which is only 0.029 $mmol{\cdot}g^{-1}$ higher than that of pure SiO_2 (0.007 $mmol{\cdot}g^{-1}$).The increase of CO_2 adsorption capacity for the 1.0CQDs/SiO_2 composites is much smaller than the enhancement observed for the CQDs/NU-1000 composites, where the capacity rose 1.11 $mmol{\cdot}g^{-1}$ (pristine NU-1000) to 1.99 $mmol{\cdot}g^{-1}$ (1.0CQDs/NU-1000). This result indicates that the enhanced CO_2 adsorption capacity in the CQDs/NU-1000 series does not stem solely from the individual contributions of CQDs; instead, it primarily originates from the interaction between CO_2 and modified NU-1000 framework. Therefore, the synergistic effect between the CQDs and the MOF framework plays a key role in improving CO_2 adsorption performance.

3.2.2. Equivalent heat of adsorption and structural stability

Based on the CO_2 adsorption isotherms at 0 °C and 25 °C, the isosteric heat of adsorption (Q_{st}) was calculated for each material, as shown in Fig. 5a. After the introduction of CQDs, the isosteric heat of CQDs/NU-1000 is higher than that of pristine NU-1000 at low CO_2 uptake. This result demonstrates that at low surface coverage, the incorporation of CQDs strengthens the affinity between CO_2 and the material, facilitating stronger adsorption. As the CO_2 uptake increases, the Q_{st} of CQDs/NU-1000 gradually decreases and finally becomes lower than that of pristine NU-1000. This indicates that at higher CO_2 adsorption capacity, the stronger adsorption sites are gradually occupied, and subsequent CO_2 molecules begin to occupy weaker adsorption sites. Consequently, the average interaction between CO_2 and the material weakens, and the differential heat released for each incremental amount of adsorbed CO_2 becomes lower. Overall, the isosteric heat mainly lie within the range of 15–35 kJ mol^{-1}, which is typical for a physisorption process [47]. The adsorption exhibits good reversibility and requires relatively low energy for regeneration. This behavior reflects an energetically heterogeneous adsorption system with multiple types of adsorption sites, where the interaction between the adsorbate and the surface predominates and the entire process is governed by physical adsorption.

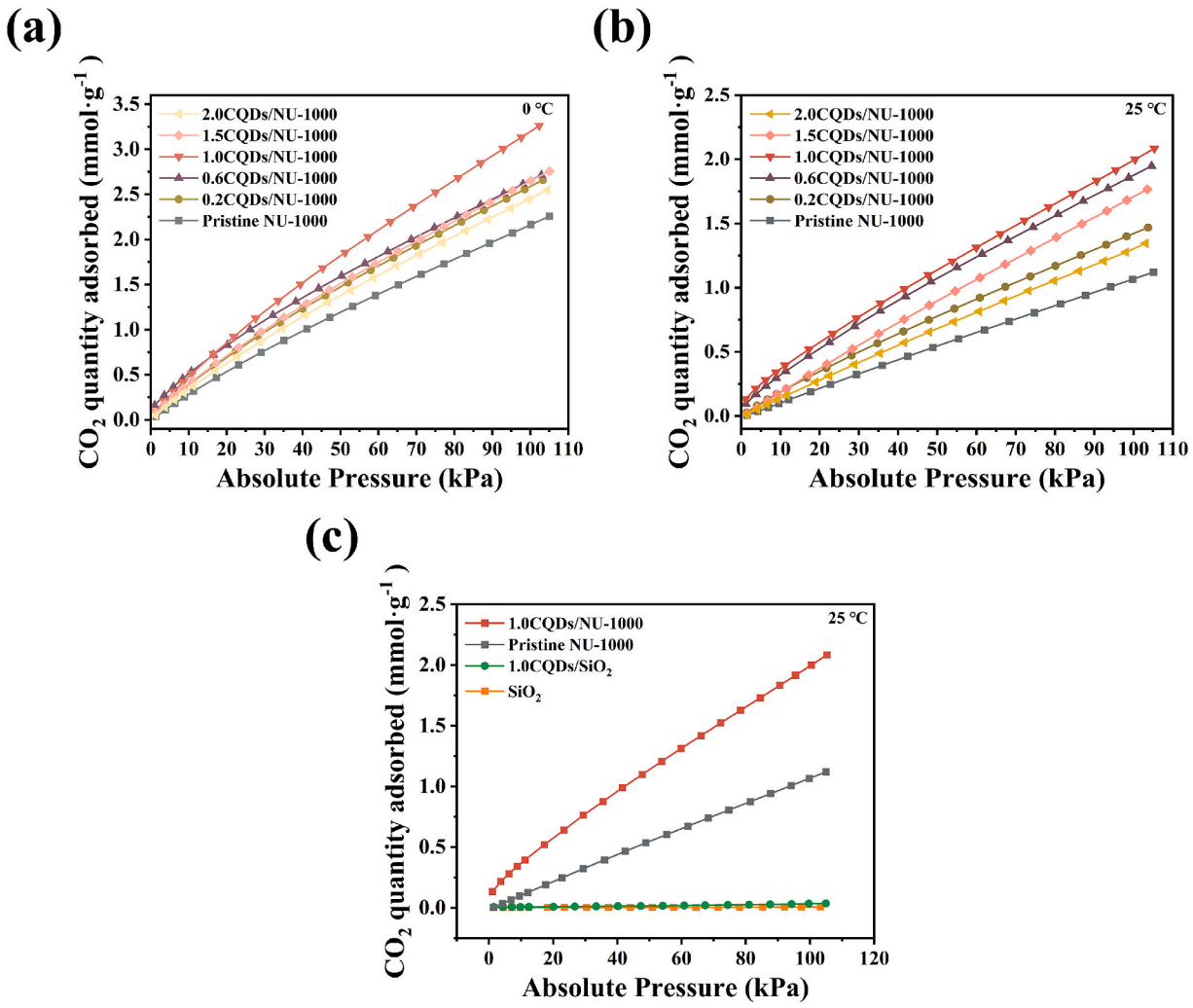

Fig. 4. Pristine NU-1000 and series of CQDs/NU-1000 CO_2 adsorption isotherm at (a) 0 °C, (b) 25 °C; (c) Comparison of pristine NU-1000 and 1.0CQDs/NU-1000, pristine SiO_2 and 1.0CQDs/SiO_2 CO_2 adsorption isotherm at 25 °C.

CO_2 temperature programmed desorption (CO_2-TPD) measurements were performed (Fig. 5b) to investigate the CO_2 adsorption strength and desorption behavior of the materials. The TPD curves show that the CO_2 desorption peaks for all samples are primarily centered 200 °C. Notably, the desorption peaks of the composites shift toward higher temperatures compared to pristine NU-1000. For the optimized 1.0CQDs/NU-1000 sample, the main desorption peak appears at 154 °C, which is significantly higher than that of pristine NU-1000. This upward shift in the desorption temperature indicates that CQDs doping strengthens the interaction between CO_2 and the material, resulting in stronger binding of CO_2 molecules [48]. The enhanced interaction contributes to increase the CO_2 adsorption capacity and thus improves overall the performance of the material in CO_2 capture and separation.

The thermal stability of pristine NU-1000 and the CQDs/NU-1000 composites was evaluated via TGA (Fig. 5c). Pristine NU-1000 exhibits two distinct stages of mass loss, corresponding to its multi-step decomposition process. In contrast, the CQDs/NU-1000 composites display a single weight-loss stage, suggesting that the incorporation of CQDs modifies and simplifies the thermal degradation pathway. Notably, the composites exhibit earlier weight loss between 150 °C and 350 °C, likely due to the accelerated removal of residual solvents and volatile species facilitated by the CQDs. However, within the 350 °C to 500 °C range, the rate of mass loss diminishes, indicating that the CQDs provide a degree of structural reinforcement to the MOF framework at elevated temperatures. This stabilization effect retards the framework collapse and ensures that the overall thermal stability of the composite remains comparable to that of pristine NU-1000. These findings suggest that, compared to pristine NU-1000, the thermal stability of CQDs-doped NU-1000 is not significantly compromised, thus justifying its suitability for multi-cycle CO_2 adsorption-desorption stability.

Fig. 5d. presents the PXRD patterns of pristine NU-1000 and the CQDs/NU-1000 composites after immersion in water for 7 days. Compared to the initial patterns (Fig. 2a), the diffraction peak intensities are significantly weakened, with certain minor peaks disappearing entirely. Notably, the characteristic peak at $2\theta = 7.4^{o}$ shifts to $2\theta = 6.6^{o}$, and a general shift toward lower angles is observed for all reflections, signifying lattice expansion and increased interplanar spacing. This phenomenon suggests that during prolonged soaking, water molecules occupy the pores and form hydrogen bonding clusters [49]. These clusters, along with the interaction between water and the hydroxyl groups on the Zr-nodes, induce structural strain that leads to the expansion of lattice parameters. Furthermore, the CO_2 adsorption performance after the 7-day water treatment was evaluated **(Fig. S4)**. The adsorption capacity decreased to 1.45 $mmol \cdot g^{-1}$, a substantial reduction from the initial value. This decline can be primarily attributed to the loss of effective adsorption sites and the partial blockage of pore channels by strongly bound water molecules. These results indicate that while the framework is largely retained, the long-term water stability of the material remains a challenge that warrants further optimization.

To quantitatively investigate the mechanism of capacity loss

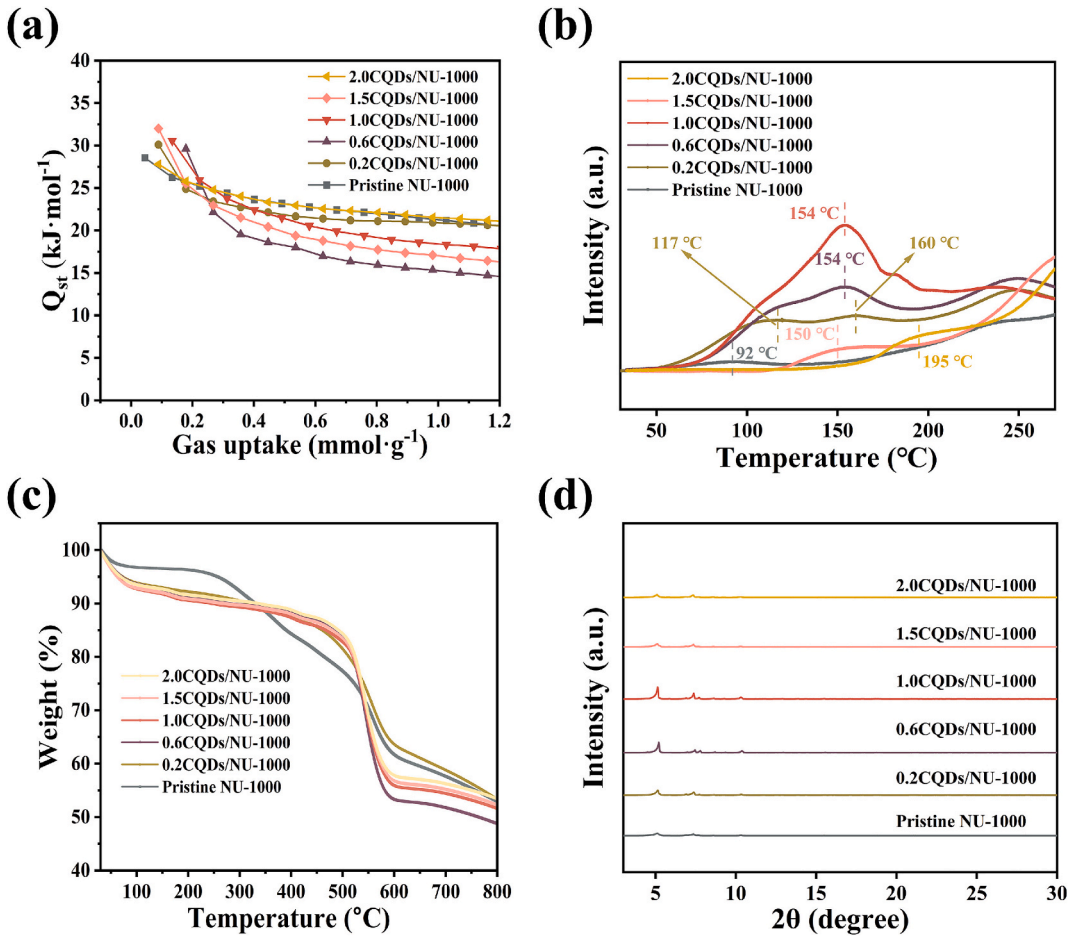

Fig. 5. Pristine NU-1000 and series of CQDs/NU-1000 (a) Equivalent adsorption heat curves, (b) CO_2-TPD curves, (c) TGA curves (d) XRD pattern after 7 days of soaking in water.

following the 7-day water soaking test, PXRD and N_2 physisorption analyses were performed (**Tables S2 and S3**). Quantitative PXRD peak integration indicates that the relative crystallinity of all samples dropped to below 50% after soaking. Subsequently, N_2 physisorption was conducted on the soaked samples after standard thermal reactivation. Because the reactivation process thoroughly removes any physically adsorbed water molecules from the pores, the physisorption results reflect the intrinsic structural state of the materials. The data reveals a permanent pore volume loss, with the BET surface area of the pristine NU-1000 and 1.0CQDs/NU-1000 composite decreased to 579 and 675 m^2g^{-1}, respectively. These results objectively confirm that prolonged exposure to liquid water induces irreversible structural collapse rather than reversible pore blockage.

To further evaluate the practical potential and water stability of the prepared materials, CO_2 adsorption performances were investigated after exposing the samples to various relative humidity levels from 0% to 100% RH for 12 h (Fig. 6 **and Table S5)**. It can be observed that as the humidity increases, the CO_2 adsorption capacity of both samples

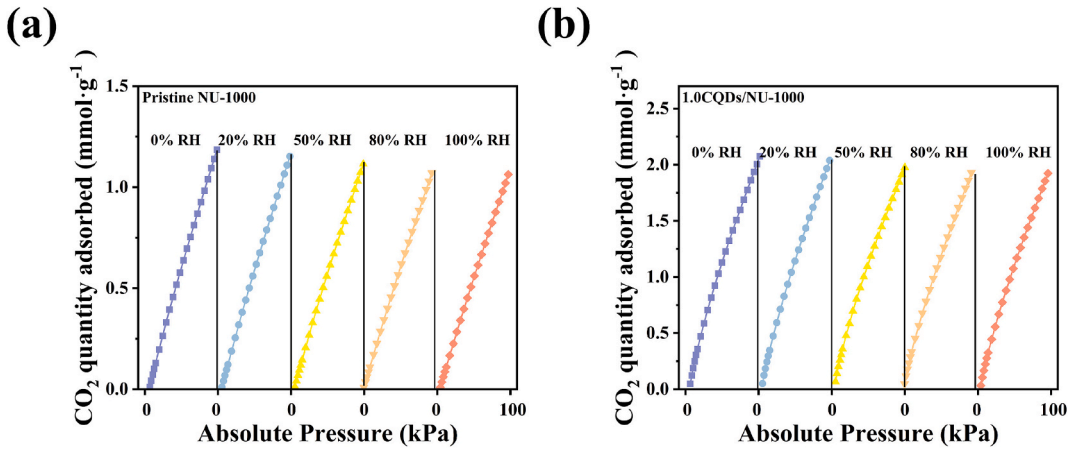

Fig. 6. A comparison of CO_2 adsorption capacities for (a) Pristine NU-1000 and (b) 1.0CQDs/NU-1000 under different relative humidity conditions at 25 °C.

exhibits a slight downward trend. This phenomenon is in high accordance with the results reported in recent studies using dynamic breakthrough measurements [14,15], which is primarily attributed to the competitive adsorption between water vapor and CO_2 molecules on the active sites.

Specifically, the 1.0CQDs/NU-1000 composite still maintains a high CO_2 adsorption capacity even under high humid conditions. For instance, it maintains an impressive adsorption capacity of 1.89 mmol·g^{-1} at 100% RH, which is 94.5% of its initial capacity under dry conditions (2.00 mmol·g^{-1}). These results demonstrate that the robust Zr-based framework of NU-1000, combined with the structural integrity of the CQDs/NU-1000 composite, provides excellent resistance to moisture interference and ensures high CO_2 capture efficiency in humid environments.

3.2.3. CO_2 adsorption cycling test

Evaluating the stability of adsorbents during cyclic adsorption-desorption processes is an important criterion. In practical applications, adsorbents must not only exhibit high CO_2 adsorption capacity but also demonstrate excellent cyclic adsorption-desorption performance. In this study, pristine NU-1000 and the best-performing 1.0CQDs/NU-1000 were tested for 10 adsorption-desorption cycles at an adsorption temperature of 25 °C and desorption temperature of 120 °C (vacuum desorption), as shown in Fig. 7.

It can be clearly observed that the CO_2 cyclic adsorption capacity of the materials fluctuates within a certain range. For the pristine material, the adsorption capacity exhibits a slight increase after 10 cycles (Fig. 7a). The pores of adsorbents are partially blocked during the first CO_2 adsorption cycle, which is attributed to the presence of the high-boiling-point solvent DMF during the synthesis process. The residual solvent molecules within the pores were gradually eliminated as the number of cycles increased, resulting in the activation of NU-1000 (V_{total} of NU-1000 from 1.23 to 1.43 cm^3/g) [45].

Conversely, the adsorption capacity of the 1.0CQDs/NU-1000 decreased from 1.95 mmol·g^{-1} to 1.70 mmol·g^{-1}, a reduction of 12.8% (Fig. 7b). Regarding the degradation of 1.0CQDs/NU-1000, we propose a mechanism of pore blockage by irreversible species. Firstly, no significant difference was observed between the TG curves of 1.0CQDs/NU-1000 before and after the 10 adsorption-desorption cycles test (Fig. 7d), which indicates CQDs might not be the main reason for the performance degradation of 1.0CQDs/NU-1000.Secondly, the specific surface area **(Table S4)** of the CQDs/NU-1000 composite after cyclic tests decreased significantly from 1937 to 1458 m^2/g, which confirms that the 120 °C activation condition is insufficient to remove the strongly bound carbonate species originating from the metal nodes and hydroxyl groups, Together with the more severe accumulation of carbonate species observed in the in-situ FTIR spectra (Fig. 9c and d) of 1.0CQDs/NU-1000, these species likely lead to the blockage of pores (V_{total} of 1.0CQDs/NU-1000 from 1.53 to 1.41 cm^3/g) and the performance degradation of 1.0CQDs/NU-1000.

In summary, while the cyclic adsorption performance of pristine NU-1000 remains effective, the doped material shows a slight decrease in cyclic adsorption performance. However, the doped material still maintains a relatively high adsorption capacity compared to its initial adsorption capacity.

3.2.4. CO_2 dynamic adsorption performance

For a more detailed evaluation of the CO_2 capture performance in

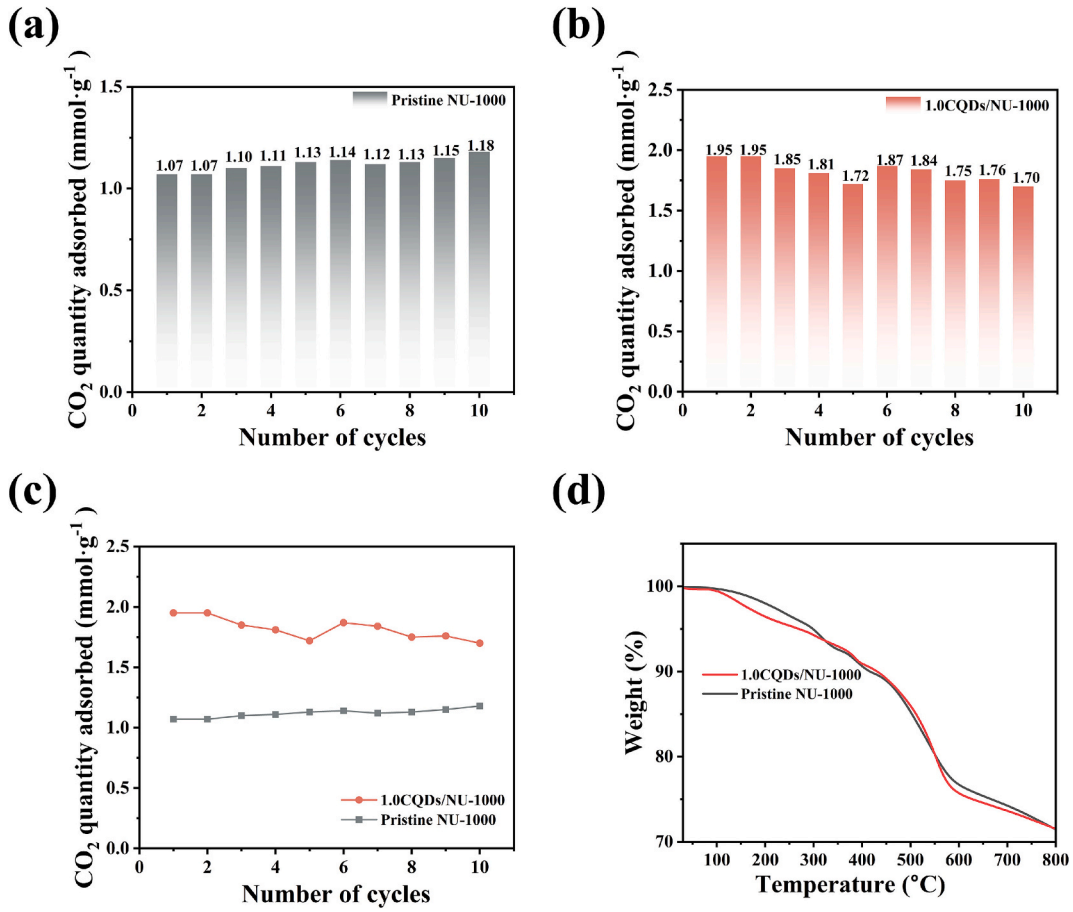

Fig. 7. 10-cycle CO_2 adsorption of (a) pristine NU-1000. (b) 1.0CQDs/NU-1000 (c) Comparison of pristine NU-1000 and 1.0CQDs/NU-1000 after 10-cycle CO_2 adsorption (d) TG curves of pristine NU-1000 and 1.0CQDs/NU-1000 after 10-cycle CO_2 adsorption.

DAC applications, dynamic breakthrough tests were conducted under simulated air conditions. After the activation of the sample in the reaction column, it was exposed to a gas mixture containing 400 ppm CO_2, 20% O_2, and the remainder N_2. The dynamic breakthrough curves were obtained by monitoring the outlet CO_2 concentration over time, as shown in Fig. 8a and b. CO_2 uptake was calculated through numerical integration of the monitored outlet concentrations, and the results are shown in Fig. 8c and d, with the integration results listed in Table 3.

From the CO_2 breakthrough curves, it is clear that the CO_2 capture capacity of the adsorbent is closely related to the breakthrough time. After the introduction of CQDs, the 1.0CQDs/NU-1000 composite exhibited a significantly longer breakthrough time compared to pristine NU-1000, indicating a higher CO_2 adsorption capacity. The longer adsorption duration time suggests that the material has a larger capacity for DAC. Based on the numerical integration of the breakthrough curves (Table 3), the CO_2 adsorption capacity of 1.0CQDs/NU-1000 is 0.025 mmol·g^{-1}, which is five times higher than the 0.005 mmol·g^{-1} capacity of pristine NU-1000, indicating a significant improvement in its DAC performance. Compared to the static adsorption isotherm data, the introduction of CQDs results in a significant increase in both dynamic breakthrough and static adsorption capacities.

Furthermore, the breakthrough curve of 1.0CQDs/NU-1000 exhibited a two-step profile, whereas pristine NU-1000 showed only a single step. This change in the CO_2 adsorption process suggests that the modified material may have introduced new adsorption sites [50]. During the adsorption process, CO_2 first enters the MOF pores through physical adsorption, and as the CO_2 concentration reaches a certain level, chemical interaction begins to take effect. CO_2 interacts with surface active sites, allowing the material to capture more CO_2 and thereby increasing the overall adsorption capacity.

Using the separation factor Eq. [51], we calculated the dynamic breakthrough selectivity (**Table S1**). The CO_2/N_2 dynamic separation factor of pristine NU-1000 was 6.56, while for 1.0CQDs/NU-1000, it increased to 25.79. This significant increase in the separation factor indicates that the CQDs doping strategy not only improves CO_2 adsorption capacity but also enhances CO_2/N_2 selectivity, making it a promising material for CO_2 capture applications, particularly in gas separation processes. The results in **Table S6** reveals that the 1.0CQDs/NU-1000 nanocomposite exhibits superior CO_2 adsorption capacity as well as textural properties compared to other MOFs previously reported MOFs.

Table 3
The dynamic adsorption performance of samples.

Samples	Gas	Adsorption capacity (mmol·g^{-1})
Pristine NU-1000	CO_2	0.0050
	N_2	1.9257
	O_2	0.5321
1.0CQDs/NU-1000	CO_2	0.0253
	N_2	2.4565
	O_2	0.8233

3.3. Mechanism of CQDs enhance CO_2 adsorption capacity

Under the same CO_2 atmosphere and test conditions, this study continuously tracked the infrared spectral evolution of the two materials over the same adsorption duration (Fig. 9). The results show that, as the CO_2 adsorption time was progressively extended, both the pristine NU-1000 and 1.0CQDs/NU-1000 materials exhibits distinct characteristic absorption peaks in the 2300–2380 cm^{-1} wavenumber range (Fig. 9a and b). This wavenumber range corresponds to the asymmetric stretching vibration mode of CO_2 molecules [52,53]. The appearance of these absorption peaks directly confirms that CO_2 molecules are

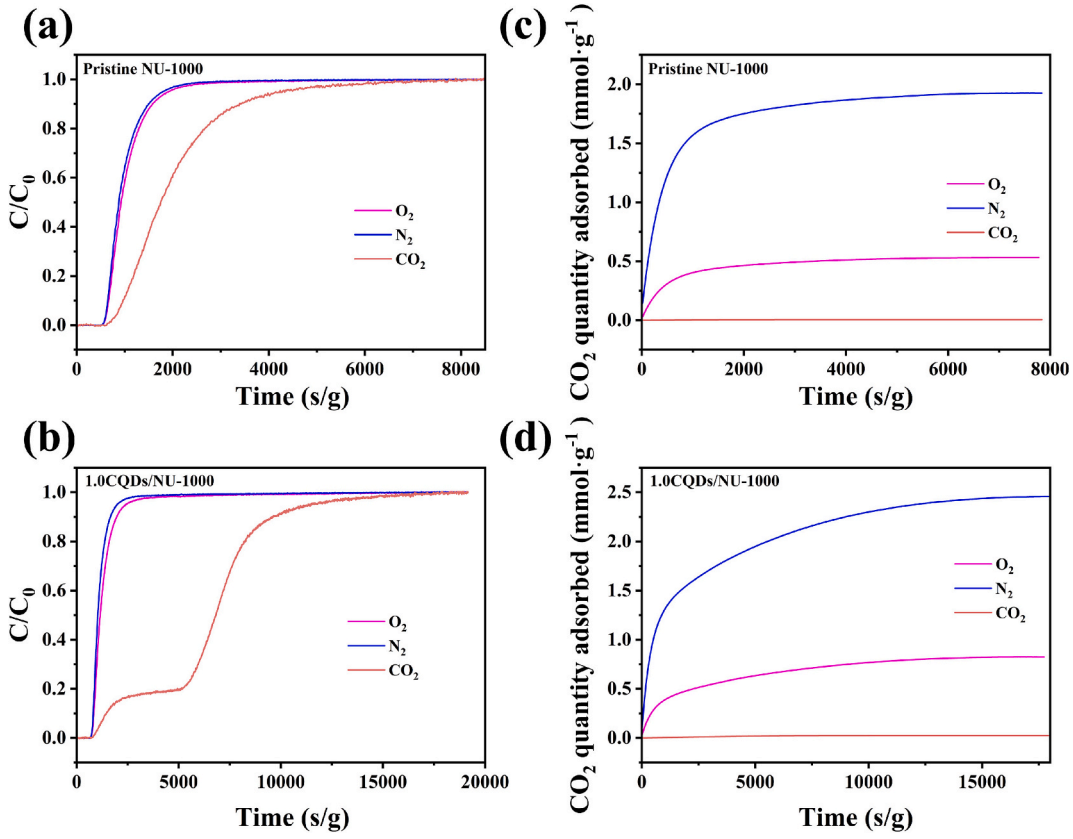

Fig. 8. Dynamic breakthrough curves of a ternary gas mixture (simulated air atmosphere with $CO_2/N_2/O_2$) for (a) pristine NU-1000 and (b) 1.0CQDs/NU-1000; dynamic CO_2 adsorption capacities of (c) pristine NU-1000 and (d) 1.0CQDs/NU-1000.

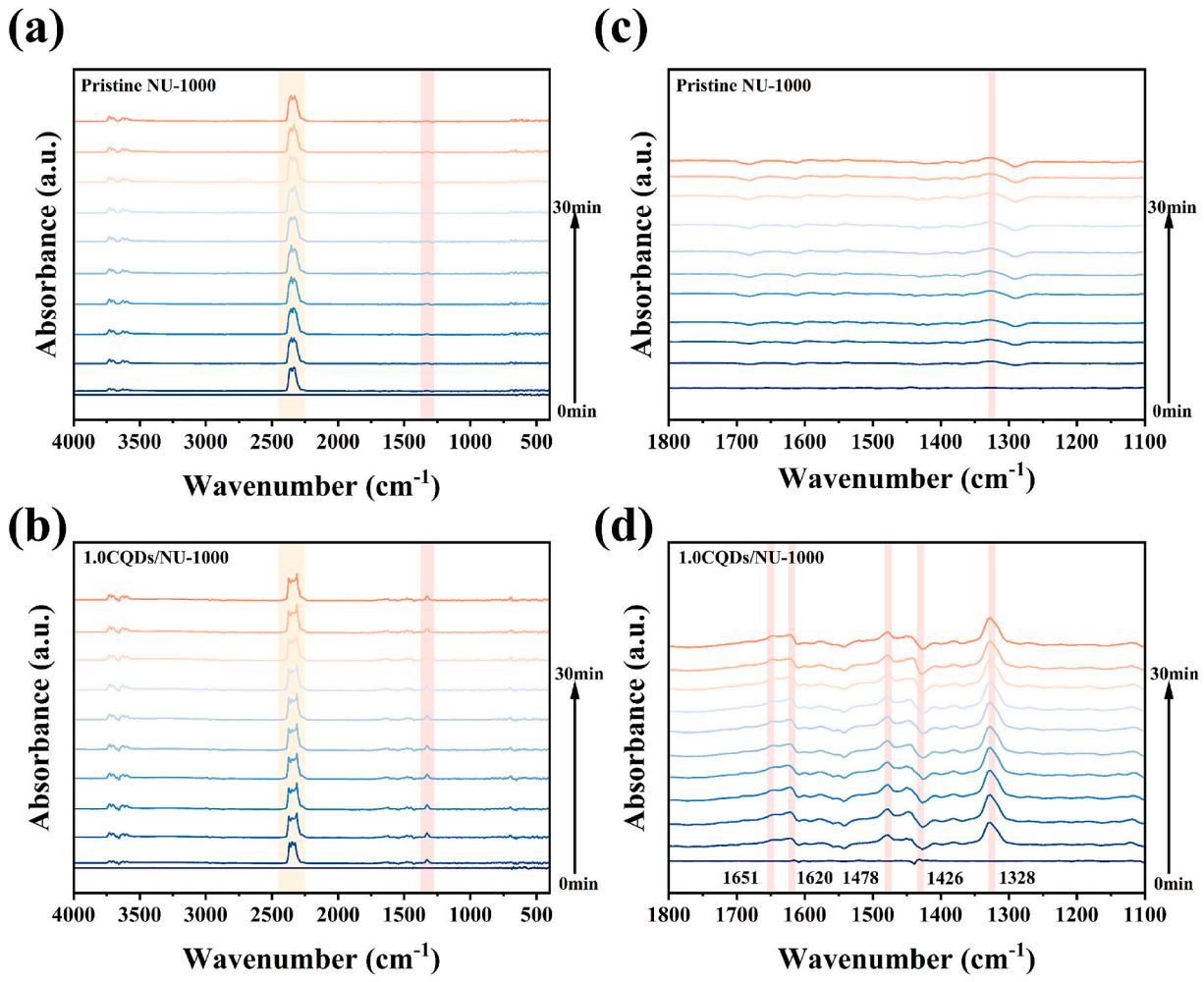

Fig. 9. In-situ FTIR spectra of pristine NU-1000(a) and (c);1.0CQDs/NU-1000(b) and (d) during CO_2 adsorption process.

successfully adsorbed onto the surfaces of both materials, and the adsorption process is mainly governed by intermolecular van der Waals forces, which is characteristic of physical adsorption.

It is noteworthy that, compared to the spectrum of the pristine NU-1000 material (Fig. 9c), the infrared spectrum of the 1.0CQDs/NU-1000 composite material, in addition to the physical adsorption characteristic peaks, also exhibits a series of new absorption peaks at 1651, 1620, 1478, 1426, and 1328 cm^{-1} (Fig. 9d). These absorption peaks are attributed to carbonate species formed on the material surface. This finding provides strong evidence that there is a chemical interaction between the 1.0CQDs/NU-1000 composite material and CO_2 molecules, in addition to physical adsorption. Specifically, the absorption peaks at 1651 and 1478 cm^{-1} correspond to the vibration modes of monodentate carbonates (m-CO_3^{2-}), whose stability is derived from the coordination bond formed between a single oxygen atom in CO_2 and the metal active sites on the material surface [54]. The absorption peaks at 1620, 1426, and 1328 cm^{-1} correspond to bidentate carbonates (b-CO_3^{2-}), which form when CO_2 molecules coordinate with multiple adjacent metal sites in a bridged manner, resulting in a more stable bridged structure [55]. The coexistence of these two carbonate species demonstrates that the 1.0CQDs/NU-1000 composite material exhibits a diverse chemical adsorption pathway for CO_2 molecules.

Based on the experimental observations and analysis, it can be concluded that the enhanced chemical adsorption performance of the 1.0CQDs/NU-1000 composite material for CO_2 is primarily attributed to the synergistic mechanism developed within the material. On the one hand, the enhanced alkalinity of the metal active sites in the material strengthens the adsorption of acidic CO_2 through Lewis acid-base interactions. On the other hand, the hydroxyl groups distributed around the metal active sites react with CO_2 and enhance the affinity for CO_2 via Lewis acid-base interactions and hydrogen bonding, thus forming carbonate species [56]. This further optimizes the chemical microenvironment of the adsorption sites, thereby significantly enhancing the interaction between the material and CO_2 molecules.

Based on the integrated results from BET, XPS, and CO_2-TPD analyses, it can be concluded that the increased CO_2 adsorption capacity arises from the enhancement of both physical and chemical adsorption processes (See Scheme 2). First, BET analysis demonstrates that the introduction of CQDs increases the surface roughness and specific surface area of the material, which promotes physical CO_2 adsorption. The larger surface area provides more active sites for CO_2 molecules, leading to an overall improvement in adsorption capacity. Second, XPS analysis reveals that after CQDs impregnation, The electron transfer from the electron-rich CQDs to the NU-1000, the basicity of Zr atoms is enhanced, favoring CO_2 adsorption at the metal sites. Additionally, the increased surface hydroxyl content promotes the formation of carbonates under CO_2 exposure. This is further supported by the CO_2-TPD results, where the desorption peaks shift to higher temperatures, indicating stronger chemical adsorption of CO_2. Thus, the incorporation of CQDs into NU-1000 is demonstrated to be an effective modification method to improve the CO_2 adsorption performance, offering a promising modification strategy for CO_2 capture applications.

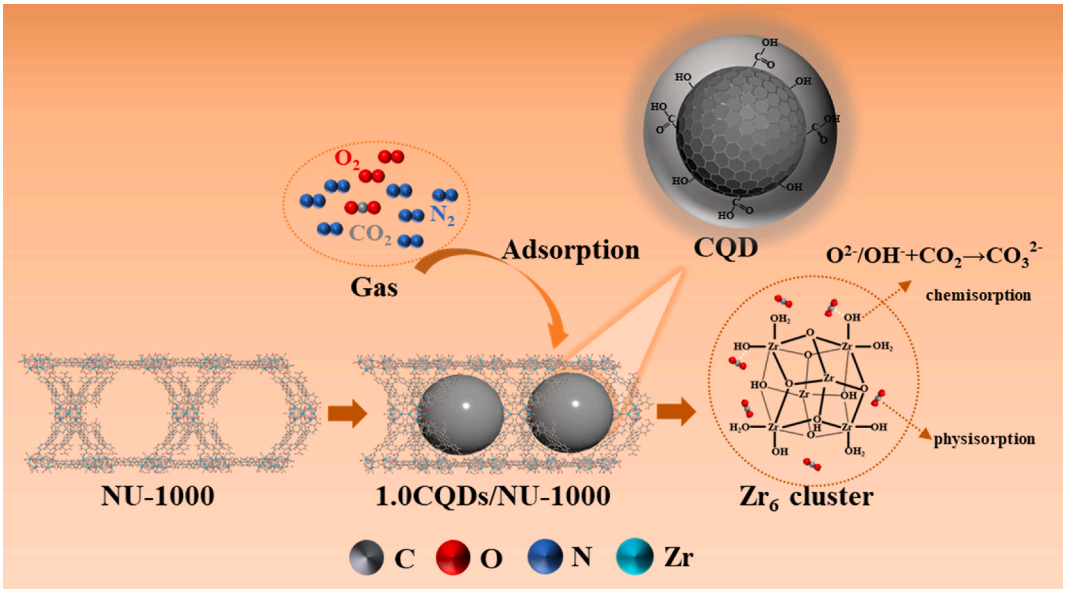

Scheme 2. Schematic illustration of the adsorption mechanism of the CQDs/NU-1000 composite.

4. Conclusion

In summary, we successfully doped CQDs into the NU-1000 metal-organic framework to form a CQDs/NU-1000 composite and further explored the interaction mechanism between CQDs and NU-1000, as well as the CO_2 adsorption enhancement mechanism. Through CO_2 static adsorption isotherms and dynamic breakthrough experiments under simulated air conditions, we found that doping with CQDs effectively improved CO_2 adsorption capacity and CO_2/N_2 dynamic breakthrough selectivity. Combining the experimental results from BET, XPS, and in situ FTIR, the introduction of CQDs enhanced both the physical and chemical CO_2 adsorption properties by increasing the specific surface area, altering the basicity of the metal sites, and increasing the surface hydroxyl oxygen content. This study demonstrates that CQDs doping is an effective modification strategy that can significantly enhance the CO_2 adsorption performance of MOFs materials, providing new insights for the design of high-performance CO_2 capture materials.

Declaration of competing interest

The authors declare that they have no known competing financial interests or personal relationships that could have appeared to influence the work reported in this paper.

Acknowledgements

This work is supported by the Natural Science Foundation of Shanghai(22ZR1471800) and the National Natural Science Foundation of China(52072387).

Appendix A. Supplementary data

Supplementary data to this article can be found online at https://doi.org/10.1016/j.seppur.2026.137682.

Data availability

Data will be made available on request.

References

[1] L.J.R. Nunes, The rising threat of atmospheric CO_2: a review on the causes, impacts, and mitigation strategies, Environments 10 (2023) 66, https://doi.org/10.3390/environments10040066.
[2] Z. Jin, C. Zhang, Five grand challenges for decarbonization of China's energy system, Natl. Sci. Rev. 12 (2025) nwaf035, https://doi.org/10.1093/nsr/nwaf035.
[3] I. Ghiat, A. Banu, Y. Bicer, A.I. Amhamed, T. Al-Ansari, Circularity within carbon capture networks: a review of capture and utilization technologies, J. CO2 Util. 95 (2025) 103075, https://doi.org/10.1016/j.jcou.2025.103075.
[4] K.S. Lackner, Capture of carbon dioxide from ambient air, Eur. Phys. J. Spec. Top. 176 (2009) 93–106, https://doi.org/10.1140/epjst/e2009-01150-3.
[5] E.S. Sanz-Pérez, C.R. Murdock, S.A. Didas, C.W. Jones, Direct capture of CO_2 from ambient air, Chem. Rev. 116 (2016) 11840–11876, https://doi.org/10.1021/acs.chemrev.6b00173.
[6] E. Hanson, C. Nwakile, V.O. Hammed, Carbon capture, utilization, and storage (CCUS) technologies: evaluating the effectiveness of advanced CCUS solutions for reducing CO_2 emissions, Results Surf. Interfaces 18 (2025) 100381, https://doi.org/10.1016/j.rsurfi.2024.100381.
[7] Y. Zhou, F. Xie, D. Wang, Y. Wang, M. Wu, Carbon capture, utilization and storage (CCUS) pipeline steel corrosion failure analysis: a review, Eng. Fail. Anal. 155 (2024) 107745, https://doi.org/10.1016/j.engfailanal.2023.107745.
[8] X. Kong, J. Wu, S. Ming, C. Cheng, Q. Wu, Y. Wang, X. Li, L. Pang, Y. Guo, T. Li, Unveiling specific CO_2 trapping sites within MOR zeolite for promoting direct air capture of CO_2, Chem. Eng. J. 506 (2025) 159855, https://doi.org/10.1016/j.cej.2025.159855.
[9] P.B. Ramos, A. Mamani, M.F. Sardella, A. Arencibia, R. Sanz, E.S. Sanz-Pérez, M. A. Bavio, M. Erans, Olive mill waste-derived activated carbon for CO_2 capture using realistic conditions, Energy Fuel 39 (2025) 5442–5452, https://doi.org/10.1021/acs.energyfuels.4c04880.
[10] K.S. Song, P.W. Fritz, A. Coskun, Porous organic polymers for CO_2 capture, separation and conversion, Chem. Soc. Rev. 51 (2022) 9831–9852, https://doi.org/10.1039/D2CS00727D.
[11] X. Wang, H. Liu, J. Zhang, S. Chen, Covalent organic frameworks (COFs): a promising CO_2 capture candidate material, Polym. Chem. 14 (2023) 1293–1317, https://doi.org/10.1039/D2PY01350A.
[12] S. Bose, D. Sengupta, T.M. Rayder, X. Wang, K.O. Kirlikovali, A.K. Sekizkardes, T. Islamoglu, O.K. Farha, Challenges and opportunities: Metal–Organic frameworks for direct air capture, Adv. Funct. Mater. (2023) 2307478, https://doi.org/10.1002/adfm.202307478.
[13] A. Kumar, D.G. Madden, M. Lusi, K. Chen, E.A. Daniels, T. Curtin, J.J. Perry, M. J. Zaworotko, Direct air capture of CO_2 by physisorbent materials, Angew. Chem. Int. Ed. 54 (2015) 14372–14377, https://doi.org/10.1002/anie.201506952.
[14] G. Zhao, T. Zhang, S. Zhang, H. Zhao, Amino-functionalized metal–organic framework fiber membranes for CO_2 adsorption, Inorg. Chem. 64 (2025) 19924–19931, https://doi.org/10.1021/acs.inorgchem.5c04074.
[15] H. Zhao, T. Zhang, S. Chen, G. Zhao, Hierarchical fibrous metal–organic framework/ionic liquid membranes for efficient CO_2 /N_2 separation, Nano Lett. 25 (2025) 2647–2654, https://doi.org/10.1021/acs.nanolett.4c05232.
[16] H. Zhao, G. Zhao, Fibrous metal–organic framework membranes with hierarchical porous channels for efficient carbon dioxide capture, ACS Appl. Mater. Interfaces (2026), https://doi.org/10.1021/acsami.5c23215.

[17] C. Xiao, J. Tian, Q. Chen, M. Hong, Water-stable metal–organic frameworks (MOFs): rational construction and carbon dioxide capture, Chem. Sci. 15 (2024) 1570–1610, https://doi.org/10.1039/D3SC06076D.

[18] C. Simari, Nanomaterials for direct air capture of CO_2: current state of the art, Challenges Future Perspectives, Mol. 30 (2025) 3048, https://doi.org/10.3390/molecules30143048.

[19] J.H. Cavka, S. Jakobsen, U. Olsbye, N. Guillou, C. Lamberti, S. Bordiga, K. P. Lillerud, A new zirconium inorganic building brick forming metal organic frameworks with exceptional stability, J. Am. Chem. Soc. 130 (2008) 13850–13851, https://doi.org/10.1021/ja8057953.

[20] H. Furukawa, F. Gándara, Y.-B. Zhang, J. Jiang, W.L. Queen, M.R. Hudson, O. M. Yaghi, Water adsorption in porous metal–organic frameworks and related materials, J. Am. Chem. Soc. 136 (2014) 4369–4381, https://doi.org/10.1021/ja500330a.

[21] J.E. Mondloch, W. Bury, D. Fairen-Jimenez, S. Kwon, E.J. DeMarco, M.H. Weston, A.A. Sarjeant, S.T. Nguyen, P.C. Stair, R.Q. Snurr, O.K. Farha, J.T. Hupp, Vapor-phase metalation by atomic layer deposition in a Metal–Organic framework, J. Am. Chem. Soc. 135 (2013) 10294–10297, https://doi.org/10.1021/ja4050828.

[22] C. Jia, T. He, G.-M. Wang, Zirconium-based metal-organic frameworks for fluorescent sensing, Coord. Chem. Rev. 476 (2023) 214930, https://doi.org/10.1016/j.ccr.2022.214930.

[23] R. Abazari, S. Sanati, M.A. Bajaber, M.S. Javed, P.C. Junk, A.K. Nanjundan, J. Qian, D.P. Dubal, Design and advanced manufacturing of NU-1000 Metal–Organic frameworks with future perspectives for environmental and renewable energy applications, Small 20 (2024) 2306353, https://doi.org/10.1002/smll.202306353.

[24] X. Li, K. Gao, B. Mo, J. Tang, J. Wu, H. Hou, BiOI particles confined into Metal–Organic framework NU-1000 for valid photocatalytic hydrogen evolution under visible-light irradiation, Inorg. Chem. 60 (2021) 1352–1358, https://doi.org/10.1021/acs.inorgchem.0c02423.

[25] H. Xue, Z.-H. Zhao, P.-Q. Liao, X.-M. Chen, Ship-in-a-bottle integration of Ditin(IV) sites into a Metal–Organic framework for boosting electroreduction of CO_2 in acidic electrolyte, J. Am. Chem. Soc. 145 (2023) 16978–16982, https://doi.org/10.1021/jacs.3c05023.

[26] F.P. Kinik, A. Ortega-Guerrero, D. Ongari, C.P. Ireland, B. Smit, Pyrene-based metal organic frameworks: from synthesis to applications, Chem. Soc. Rev. 50 (2021) 3143–3177, https://doi.org/10.1039/D0CS00424C.

[27] H. Liu, D. Si, M.F. Smith, R. Li, X. Li, L. Li, H. Huang, Z. Fang, H. Zhou, T. Liu, Efficient CO_2 photoreduction enabled by the energy transfer pathway in metal-organic framework, Aggregate 4 (2023) e383, https://doi.org/10.1002/agt2.383.

[28] Y. Zhang, L. Ding, Z. Xie, X. Zhang, X. Sui, J.-R. Li, Porous sorbents for direct capture of carbon dioxide from ambient air, Chin. Chem. Lett. (2024) 109676, https://doi.org/10.1016/j.cclet.2024.109676.

[29] L. Qiu, N. Mokhtarinori, H. Liu, D. Jiang, Z. Yang, S. Dai, The carbon challenge: design, synthesis, and chemisorption behavior of solid sorbents in direct air capture of carbon dioxide, Mater. Today Energy 47 (2025) 101740, https://doi.org/10.1016/j.mtener.2024.101740.

[30] F. Sher, A. Hayward, A. El Guerraf, B. Wang, I. Ziani, H. Hrnjić, E. Boškailo, A. Chupin, M.R. Nemţanu, Advanced metal–organic frameworks for superior carbon capture, high-performance energy storage and environmental photocatalysis–a critical review, J. Mater. Chem.A 12 (2024) 27932–27973, https://doi.org/10.1039/D4TA03877K.

[31] C. Zhou, H. Li, H. Qin, B. Yuan, M. Zhang, L. Wang, B. Yang, C. Tao, S. Zhang, Defective UiO-66-NH_2 monoliths for optimizing CO_2 capture performance, Chem. Eng. J. 467 (2023) 143394, https://doi.org/10.1016/j.cej.2023.143394.

[32] S. Assyl, S. Botakoz, Z. Saule, Dimensions, structure, and morphology variations of carbon-based materials for hydrogen storage: a review, Discov. Nano 20 (2025) 115, https://doi.org/10.1186/s11671-025-04229-3.

[33] K. Sonowal, N. Nandal, P. Basyach, L. Kalita, S.L. Jain, L. Saikia, Photocatalytic reduction of CO_2 to methanol using Zr(IV)-based MOF composite with g-C_3N_4 quantum dots under visible light irradiation, J. CO2 Util. 57 (2022) 101905, https://doi.org/10.1016/j.jcou.2022.101905.

[34] S. Li, K. Ji, M. Zhang, C. He, J. Wang, Z. Li, Boosting the photocatalytic CO_2 reduction of metal–organic frameworks by encapsulating carbon dots, Nanoscale 12 (2020) 9533–9540, https://doi.org/10.1039/D0NR01696A.

[35] S. Fakhraie, H.R. Rajabi, E. Ghasemy, A. Rashidi, Y. Orooji, M.H. Hadizadeh, D. Maklavany, Exceptional CO_2 and H_2S adsorption by tuning micro/mesopore ratios with embedded graphene oxide/n-doped carbon quantum dots in MIL-101 (Cr): experimental and computational insights, J. Colloid Interface Sci. 683 (2025) 769–783, https://doi.org/10.1016/j.jcis.2024.12.211.

[36] J. Yu, X. Wang, L. Chen, G. Lu, G. Shi, X. Xie, Y. Wang, J. Sun, Enhanced adsorption and visible-light photocatalytic degradation of toluene by CQDs/UiO-66 MOG with hierarchical pores, Chem. Eng. J. 435 (2022) 135033, https://doi.org/10.1016/j.cej.2022.135033.

[37] T.C. Wang, N.A. Vermeulen, I.S. Kim, A.B.F. Martinson, J.F. Stoddart, J.T. Hupp, O. K. Farha, Scalable synthesis and post-modification of a mesoporous metal-organic framework called NU-1000, Nat. Protoc. 11 (2016) 149–162, https://doi.org/10.1038/nprot.2016.001.

[38] M. Farshbaf, S. Davaran, F. Rahimi, N. Annabi, R. Salehi, A. Akbarzadeh, Carbon quantum dots: recent progresses on synthesis, surface modification and applications, Artif. Cells Nanomed. Biotechnol. 46 (2018) 1331–1348, https://doi.org/10.1080/21691401.2017.1377725.

[39] J.D. Stachowska, A. Murphy, C. Mellor, D. Fernandes, E.N. Gibbons, M. J. Krysmann, A. Kelarakis, E. Burgaz, J. Moore, S.G. Yeates, A rich gallery of carbon dots based photoluminescent suspensions and powders derived by citric acid/urea, Sci. Rep. 11 (2021) 10554, https://doi.org/10.1038/s41598-021-89984-w.

[40] X. Wang, Y. Tuo, Y. Zhou, D. Wang, S. Wang, J. Zhang, Ta-doping triggered electronic structural engineering and strain effect in NiFe LDH for enhanced water oxidation, Chem. Eng. J. 403 (2021) 126297, https://doi.org/10.1016/j.cej.2020.126297.

[41] C. Zhang, H. Yin, X. Bai, Z. Yang, Ru doping induced lattice distortion of cu nanoparticles for boosting electrochemical nonenzymatic hydrogen peroxide sensing, Colloids Surf. A Physicochem. Eng. Asp. 666 (2023) 131311, https://doi.org/10.1016/j.colsurfa.2023.131311.

[42] J. Cui, Z. Qiu, L. Yang, Z. Zhang, X. Cui, H. Xing, Kinetic-sieving of carbon dioxide from acetylene through a novel sulfonic Ultramicroporous material, Angew. Chem. - Int. Ed. 61 (2022) e202208756, https://doi.org/10.1002/anie.202208756.

[43] J. Zhu, H. Wen, X. Liu, S. Zhang, J. Wang, C. He, W. Han, Y. Han, D. Yang, N. Song, Defect-induced pore engineering in HKUST-1 by N-doped graphene quantum dots for CO_2 adsorption enhancement, J. Environ. Manage. 395 (2025) 127913, https://doi.org/10.1016/j.jenvman.2025.127913.

[44] F. Song, H. Sun, H. Ma, H. Gao, Porous TiO_2/carbon dot Nanoflowers with enhanced surface areas for improving photocatalytic activity, Nanomaterials 12 (2022) 2536, https://doi.org/10.3390/nano12152536.

[45] H. Yang, J. Guo, Y. Xia, J. Yan, L. Wen, Schottky-assisted S-scheme heterojunction photocatalyst CdS/Pt@NU-1000 for efficient visible-light-driven H_2 evolution, J. Mater. Sci. Technol. 195 (2024) 155–164, https://doi.org/10.1016/j.jmst.2024.01.051.

[46] J. Gao, C. Bai, T. Zheng, G. Sun, H. Jin, X. Sun, Z. Li, P. Colombo, B. Wang, *In-situ* growth of MOFs on porous geopolymer spheres for continuous-flow PMS degradation of antibiotics, J. Adv. Ceram. 14 (2025) 9221114, https://doi.org/10.26599/JAC.2025.9221114.

[47] J. Li, W. Zhou, X. Meng, Y. Huang, X. Li, N. Xue, Z. Qu, L. Xie, J. Li, Z. Liu, Y. Fang, F. Sun, J. Gao, G. Zhao, Scalable confined-space microwave heating strategy enables the rapid preparation of N/O co-doped activated carbons with high gas capture capacity, Carbon 225 (2024) 119152, https://doi.org/10.1016/j.carbon.2024.119152.

[48] L. Lei, Y. Cheng, C. Chen, M. Kosari, Z. Jiang, C. He, Taming structure and modulating carbon dioxide (CO_2) adsorption isosteric heat of nickel-based metal organic framework (MOF-74(Ni)) for remarkable CO_2 capture, J. Colloid Interface Sci. 612 (2022) 132–145, https://doi.org/10.1016/j.jcis.2021.12.163.

[49] H.G. Palhares, A.G. Leonel, R.L. Oréfice, R.O. Correia, D. Riassetto, M. Langlet, M. Houmard, E.H.M. Nunes, Tailoring the pore architecture and crystalline structure of UiO-66 for the selective adsorption of anionic species in aqueous media, Environ. Nanotechnol. Monit. Manage. 20 (2023) 100869, https://doi.org/10.1016/j.enmm.2023.100869.

[50] P.J. Milner, J.D. Martell, R.L. Siegelman, D. Gygi, S.C. Weston, J.R. Long, Overcoming double-step CO_2 adsorption and minimizing water CO-adsorption in bulky diamine-appended variants of Mg_2 (dobpdc), Chem. Sci. 9 (2018) 160–174, https://doi.org/10.1039/C7SC04266C.

[51] S. Jiang, H. Sun, K. Gong, X. Huang, Y. Zhu, X. Feng, J. Xie, J. Liu, B. Wang, Metal-organic frameworks for breakthrough separation of 2-Butene isomers with high dynamic selectivity and capacity, Angew. Chem. Int. Ed. 62 (2023) e202302036, https://doi.org/10.1002/anie.202302036.

[52] M. Zheng, Z. Fang, W. Xue, T. Yan, H. Huang, C. Zhong, CO_2 chemical trap and electronegative microenvironment enable metal–organic framework with one-step ethylene purification from quaternary mixture, Adv. Funct. Mater. (2025) 2422135, https://doi.org/10.1002/adfm.202422135.

[53] L. Qiu, M. Lei, C. Wang, J. Hu, L. He, A.S. Ivanov, D. Jiang, H. Lin, I. Popovs, Y. Song, J. Fan, M. Li, S.M. Mahurin, Z. Yang, S. Dai, Ionic pairs-engineered fluorinated covalent organic frameworks toward direct air capture of CO_2, Small (2024) 2401798, https://doi.org/10.1002/smll.202401798.

[54] A. Lund, G.V. Manohara, A.-Y. Song, K.M. Jablonka, C.P. Ireland, L.A. Cheah, B. Smit, S. Garcia, J.A. Reimer, Characterization of chemisorbed species and active adsorption sites in Mg–Al mixed metal oxides for high-temperature CO_2 capture, Chem. Mater. 34 (2022) 3893–3901, https://doi.org/10.1021/acs.chemmater.1c03101.

[55] J. Baltrusaitis, J. Schuttlefield, E. Zeitler, V.H. Grassian, Carbon dioxide adsorption on oxide nanoparticle surfaces, Chem. Eng. J. 170 (2011) 471–481, https://doi.org/10.1016/j.cej.2010.12.041.

[56] J.H. Kang, T.-U. Yoon, S.-Y. Kim, M.-B. Kim, H.-J. Kim, H.-C. Yang, Y.-S. Bae, Extraordinarily selective adsorption of CO_2 over N_2 in a polyethyleneimine-impregnated NU-1000 material, Microporous Mesoporous Mater. 281 (2019) 84–91, https://doi.org/10.1016/j.micromeso.2019.03.001.